Monitoring and Simulation of Axial Deformation in a High-Rise Twin Tower Connected Building: Fractional Order Viscoelasticity Constitutive Method

Xianming Luo[1]; Yun Zhou[2]; Wenjie Zhang[3]; Xiaofeng Zhou[4]; and Hui He, Ph.D.[5]

Abstract: This paper investigated the influence of axial deformation on the structural behavior of a high-rise twin tower connected building during its construction. A comprehensive structural health monitoring (SHM) system was deployed, featuring embedded strain sensors within specific vertical members. The SHM system collected strain data throughout the entire construction process, facilitating a detailed analysis of axial deformation progression and variations among vertical components such as walls and columns. Through methodical simplifications and theoretical assumptions, a calculation framework employing concrete shrinkage and creep models was proposed to quantify axial deformation. A comparative analysis was conducted between the calculation results of various models and the measured data, revealing significant discrepancies in the predictions of existing models. Additionally, it was observed that many parameters in these models are challenging to obtain during the design and construction stage. Subsequently, this study introduces a novel time-varying constitutive model based on fractional calculus viscoelasticity to address complexities in existing models and parameter acquisition challenges. The model is characterized by its clear physical interpretation and concise computational parameters, calibrated utilizing measured strain data and Bayesian optimization methods, which significantly enhances prediction accuracy and simplifies the calculation process. **DOI: 10.1061/JSENDH.STENG-13973.**

Author keywords: High-rise building; Twin tower; Axial deformation; Structural health monitoring; Concrete constitutive modeling; Creep and shrinkage; Bayesian optimization.

Introduction

The development of high-rise buildings signifies an important milestone in modern architecture and engineering, driving rapid advancements in construction techniques and structural design. With the continuous increase in height and complexity of high-rise buildings, the impact of concrete creep and shrinkage characteristics on structure has become increasingly significant and cannot be ignored. In recent years, the materials used in high-rise buildings have predominantly remained steel and concrete. Concrete creep and shrinkage have historically been extensively researched in infrastructural projects such as long-span bridges (Beltempo et al. 2018; Bažant et al. 2012) and dams (Prakash et al. 2018; Kang et al. 2017; Su et al. 2015; Sortis and Paoliani 2007), primarily due to the stringent material performance requirements. The structural deformations caused by creep and shrinkage can lead to serious consequences, including loss of prestressing force, excessive deflection, cracking, and water seepage. For high-rise buildings, as the height of the structure increases, the cumulative deformations of vertical members caused by time-dependent properties of concrete can result in significant deviations from the intended design elevations at the top of the structure (Moragaspitiya et al. 2010; Jayasinghe and Jayasena 2004), which can create challenges for subsequent installations of facades, elevators, and other facilities. Furthermore, the differences in deformation of wall and column members can impose additional internal forces on adjacent structural elements, leading to structural cracking and reducing safety and durability. As a result, the axial deformations induced by concrete creep and shrinkage in high-rise structures have attracted significant attention from researchers (Gao et al. 2020; Elnimeiri and Joglekar 1989; Russell 1980; Havlásek et al. 2021).

The shrinkage and creep properties of concrete have a developmental history spanning nearly a century, resulting in various calculation formulas and models such as Model Code 2010 (MC2010) (CEB-FIP 2010), ACI 209R (ACI 1992), Bažant and Panula (BP) model (Bažant and Panula 1978), Bažant 3 (B3), Bažant 4 (B4) model (Bažant and Murphy 1996; Wendner et al. 2013), and Gardner and Lockman 2000 (GL2000) model (Gardner and Lockman 2001). However, due to the complex mechanics of concrete and the fact that most existing models are empirical or semiempirical formulas derived from regression analysis of experimental data, there have still been many experimental and theoretical studies on concrete shrinkage and creep mechanisms in recent

[1]Ph.D. Candidate, College of Civil Engineering, Hunan Univ., Changsha 410082, China. ORCID: https://orcid.org/0000-0002-8087-5565. Email: luoxianming@hnu.edu.cn

[2]Professor, Key Laboratory for Damage Diagnosis of Engineering Structures of Hunan Province, Key Laboratory of Building Safety and Energy Efficiency of the Ministry of Education, College of Civil Engineering, Hunan Univ., Changsha 410082, China (corresponding author). ORCID: https://orcid.org/0000-0003-3153-2467. Email: zhouyun05@hnu.edu.cn

[3]Postgraduate Student, College of Civil Engineering, Hunan Univ., Changsha 410082, China. Email: zhangwj29@hnu.edu.cn

[4]Ph.D. Candidate, College of Civil Engineering, Hunan Univ., Changsha 410082, China. Email: zxf1021@hnu.edu.cn

[5]Associate Professor, College of Civil Engineering, Hunan Institute of Technology, Hengyang 421002, China. ORCID: https://orcid.org/0000-0002-0732-8231. Email: hhe@hnit.edu.cn

Note. This manuscript was submitted on April 23, 2024; approved on November 7, 2024; published online on February 28, 2025. Discussion period open until July 28, 2025; separate discussions must be submitted for individual papers. This paper is part of the ***Journal of Structural Engineering***, © ASCE, ISSN 0733-9445.

years (Bal and Buyle-Bodin 2013; Gandomi et al. 2016; Shen et al. 2020; Bouras and Vrcelj 2023; Zhu and Wang 2021).

To investigate the concrete shrinkage and creep in RC vertical members during construction and their impact on high-rise structures, the American Concrete Institute (ACI) conducted a systematic study in the 1970s on long-term axial strain monitoring of vertical members in three high-rise buildings (Russell 1980; Pfeifer et al. 1971; Russell and Corley 1978). These studies demonstrated the feasibility of predicting time-dependent deformation based on existing shrinkage and creep models. Nowadays, most landmark buildings deploy structural health monitoring (SHM) systems during construction for safety assurance. For instance, Baker et al. (2007a, b) introduced the Burj Khalifa, the world's tallest building, and its SHM system, confirming the validity of existing calculation models for axial deformations caused by concrete shrinkage and creep. Li et al. (2017) conducted structural health monitoring during the construction stage of the 660-m-high Ping-An Finance Center in Shenzhen (China's current tallest building), combining on-site measurements with numerical analysis to study vertical deformations, using elevation reservation construction methods to moderately increase floor height to compensate for axial deformations. Xia et al. (2011) utilized a combination of finite-element (FE) analysis and on-site monitoring to study stress–strain development for the 610-m-high Guangzhou TV Tower. This included examining the shrinkage and creep characteristics of concrete, the strain responses under extreme events like typhoons and earthquakes, as well as stress–strain variation laws during construction. Gao et al. (2020) performed structural deformation monitoring and numerical analysis on a 335-m-high building in Wuhan, China. Their analysis compared on-site monitoring data with FE model results considering construction speed and the time-varying properties of concrete, highlighting significant effects of construction sequence and environmental humidity. Subsequently, Wang et al. (2020) predicted axial deformations of mega columns and shear walls in high-rise buildings using an improved B3 model based on humidity sensor data. Su et al. (2013) provided a detailed introduction to the structural health monitoring system of the Shanghai Tower and outlined preliminary development patterns of structural component stress–strain during construction. Glisic et al. (2013) introduced a high-rise building strain monitoring project by the Housing and Development Board (HDB) of Singapore, analyzing nearly a decade's worth of monitoring strain of vertical members from six buildings using embedded optical fiber sensors, finding that the monitoring results generally met specification requirements but lacked accurate shrinkage and creep coefficients and uncertainties in actual loads during construction.

The aforementioned study focused on monitoring and simulating the strain development of vertical members in high-rise buildings during both construction and operational stages. However, it becomes apparent that relying solely on existing codes and models for calculations often proves inadequate. The strain data are typically discontinuous, and the number of members from which strain is collected is limited, lacking the conditions for systematic summarization. Additionally, vertical members in high-rise structures typically possess larger cross-sectional areas and reinforcement ratios, significantly differing from the standard sizes of laboratory specimens used in existing shrinkage and creep calculation formulas. Furthermore, the uncertainty surrounding environmental and load conditions at construction sites is considerably higher than that encountered in controlled laboratory conditions. Hence, for an accurate assessment of axial deformation, more precise and rational models and calculation methods are imperative.

Fintel and Khan (1969) and Fintel et al. (1986) conducted early research on axial deformation and compensatory methods during the construction stage of high-rise structures, incorporating nonelastic deformations of vertical members. Pan et al. (1992) proposed a calculation method for axial deformations considering concrete shrinkage and creep based on the superposition principle. Pereira and Glisic (2023) introduced a data-driven strategy to calibrate creep and shrinkage models using SHM data, enabling predictions of axial deformation behavior in high-rise buildings. Based on extensive case studies, Jayasinghe and Jayasena (2004) identified the effects of construction sequence, speed, and concrete strength on axial deformation, facilitating consideration of these factors during preliminary design and construction stages. Sharma et al. (2004) and Maru et al. (2001) proposed a simplified procedure for evaluating creep and shrinkage effects in RC frames. In this procedure, the inelastic axial forces, which get generated progressively with time in various substructures, are assumed to arise only at an instant time. Moragaspitiya et al. (2010) developed a compression-only element placed at the top of each story in a structure to precisely quantify axial deformations under different construction stages using FE methods. Kurc and Lulec (2013) explored several commonly used structural analysis methods, and revealed that the axial loads on columns and walls could vary by as much as 45%, depending on the analysis type and considerations. Praveen Moragaspitiya et al. (2013) proposed a mothed using structural vibration characteristics to update the axial deformation during construction by establishing a relationship between dynamic stiffness's vibration properties and axial deformation of static stiffness. Zhu et al. (2019) similarly proposed an accurate and cost-effective method for measuring dynamic displacement in supertall structures by integrating acceleration and strain data from SHM systems. Kwak and Kim (2006) also conducted a time-dependent analysis on RC frame structures considering construction sequence, and the creep deformation of concrete is described in accordance with a first-order algorithm based on the expansion of a degenerated kernel of the compliance function, validated through a 10-story RC frame to verify the proposed model's effectiveness.

The mentioned studies employ various methodologies to enhance the precise calculation of axial deformations. However, most of them indicate that the development of deformation in vertical members largely depends on the construction sequence and conditions, and that the difficulty in acquiring data for these methods limits their feasibility in calculations. In terms of the constitutive relationship of concrete material, the existing models are mostly derived from regression analysis of experimental results and involve numerous parameters, many of which have minimal impact on the calculated results. This complexity poses significant challenges for designers and construction decision-making. Additionally, concrete shrinkage and creep typically occur rapidly within a short period after casting or loading, leading to initial rapid development of axial deformations during construction. However, the operational conditions during the early stages of construction present difficulties in acquiring comprehensive data. Therefore, a thorough exploration of concrete properties, along with the application throughout the entire construction process, is crucial for ensuring the structural safety and reliability of skyscrapers. Hence, conducting an in-depth study of concrete properties and investigating their developmental patterns throughout the entire structural construction process are crucial for ensuring structural safety and reliability.

This study focused on a particular high-rise twin tower connected structure with varying heights, plan layouts, load conditions, and construction progress. An SHM system was deployed during the construction process to acquire time-varying strain data of vertical members, and a constitutive relationship based on fractional calculus (FC) derivatives is proposed to efficiently characterize the time-varying deformations of the vertical members. In previous

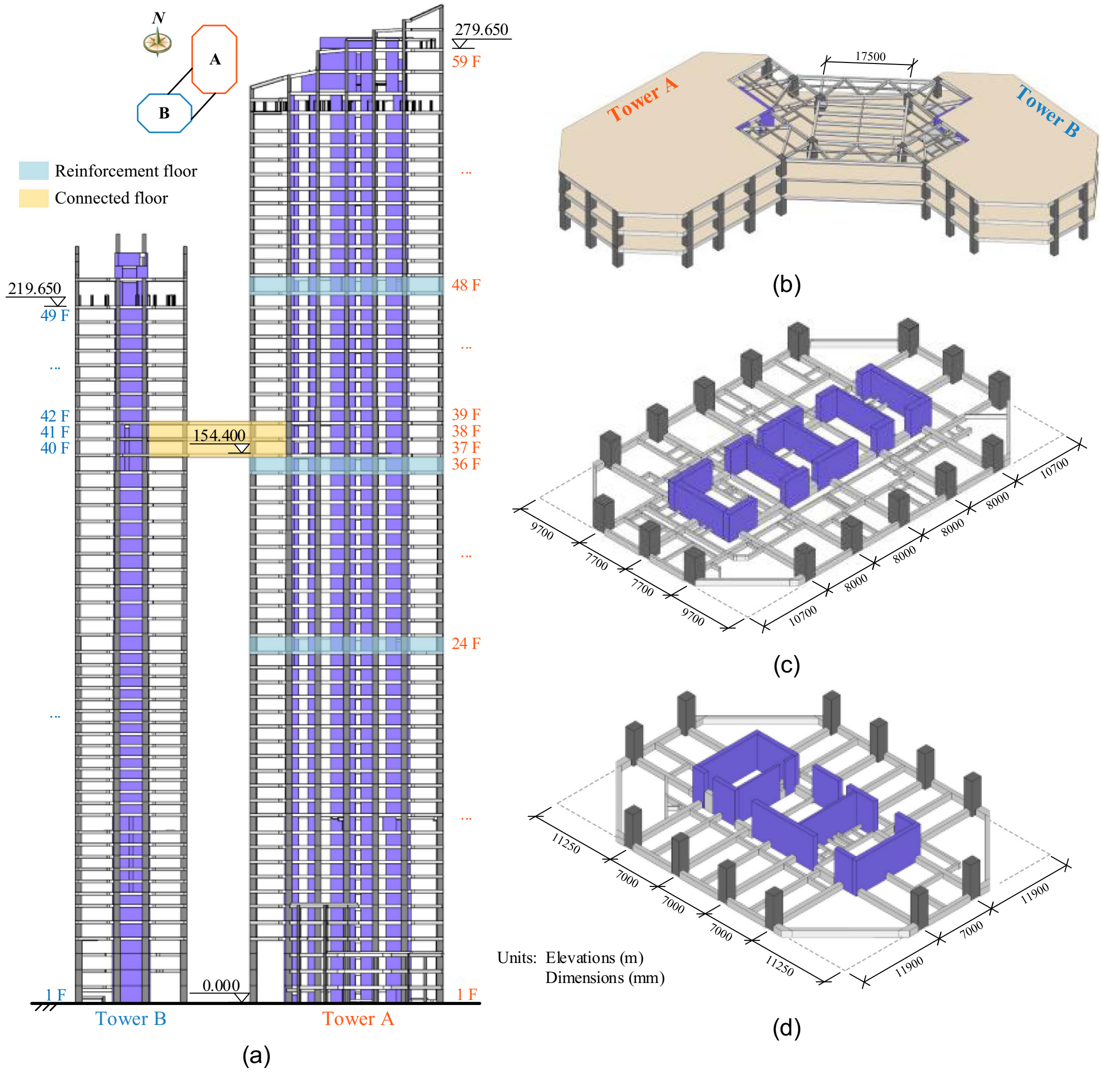

Fig. 1. Project overview: (a) elevation diagram of the structure; (b) connected floor; (c) typical floor plan of Tower A; and (d) typical floor plan of Tower B.

research, Bayesian inference (Zhou et al. 2023) and an improved Kalman filter (Zhou et al. 2024) were employed separately for preliminary analysis and discussion of strain data obtained from the SHM system. Bayesian inference was used to correct the parameters of the time-dependent calculation formula as specified in MC2010, thereby enabling better prediction of deformation development. On the other hand, the improved Kalman filter was used for filtering strain data, diagnosing anomalies, and providing monitoring warnings in the field. Despite utilizing the same case study and background, the research directions of this study diverged. Additionally, the strain data previously obtained were limited because the building had not yet been completed at that time.

Project Overview and SHM System

SNTO Meixi-Lake International Headquarters Center

The SNTO Meixi-Lake international headquarters center, located in Changsha, China, was chosen for this research. It is a high-rise twin tower connected structure. The structure consists of Tower A and Tower B, both of which are framed core tube structures and are connected by an aerial steel skybridge structure. Tower A has a building area of 96,000 m^2, with 59 floors above ground and a height of 279.65 m. Tower B covers an area of 63,000 m^2, with 49 floors and a height of 219.65 m, as shown in Fig. 1(a). The steel skybridge is positioned approximately 150 m above ground level, consisting of a three-story steel truss structure with a span of 17.5 m, as depicted in Fig. 1(b). The vertical member of the building comprises RC or steel-reinforced concrete (SRC) columns, except for the columns connecting the connected story and the steel skybridge, which are concrete-filled steel tubular (CFT) columns. Strengthening layers are implemented in Tower A at Floors 24, 36, and 48, featuring outrigger trusses to connect the core tube with the frame columns. Figs. 1(c and d) illustrate the schematic layout for a standard floor in Tower A and Tower B, respectively.

Construction Sequence

The primary structure of Tower B was initially cast on April 18, 2021, and reached its final elevation on July 19, 2023. Tower A began casting on August 21, 2021, and topped out on November 29, 2023. The steel skybridge began construction after both towers were topped out, employing a high-altitude modular assembly method. The construction progress on-site is illustrated in Fig. 2. The specific construction timelines for each floor of Tower A,

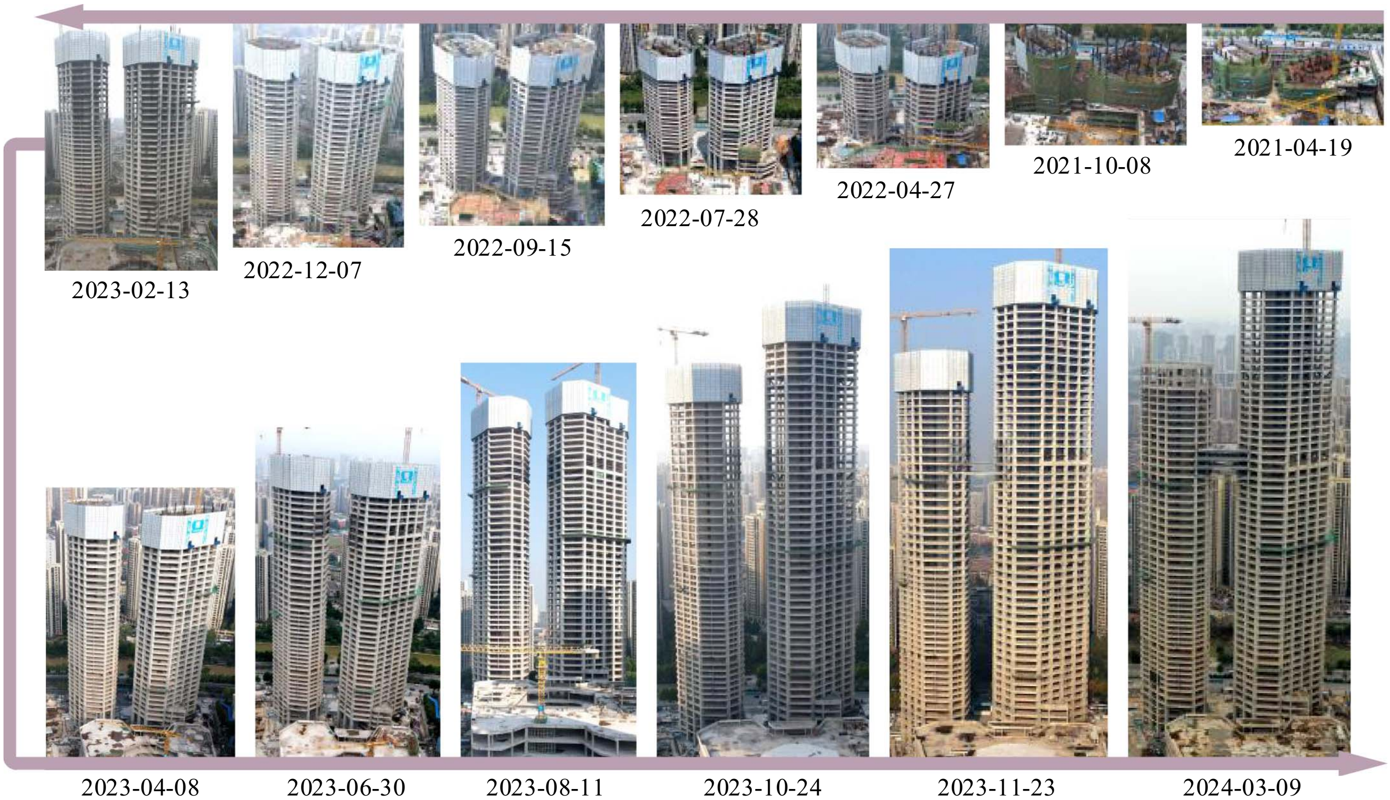

Fig. 2. Construction process. (Images by Xianming Luo.)

as well as the cumulative gravitational and construction loads per floor, are depicted in Fig. 3. During the entire construction stage, there were two periods of suspension. The structural computational model loads were adjusted to match the construction stage loads [2.5 kN/m^2 (Fan et al. 2013)]. Subsequently, the bottom axial forces of the monitored members on each floor were extracted, cumulatively representing the load at the base level. From the load variation, it is evident that, except for the Position A6, the wall load exceeds that of the columns. However, due to the significantly larger cross-sectional area of the shear walls compared to the frame columns, the axial compression ratio of the walls is noticeably lower than that of the columns. This finding is consistent with conclusions drawn from previous studies (Blanc et al. 2021). The reason for the lower wall load at Position A6 is that the wall section at this location is smaller, resulting in lower gravity loads transmitted from above.

SHM System

To accurately assess the structural performance during construction and investigate the differences in axial deformations among vertical members as well as the cumulative effect of axial deformations along the height on the construction, a comprehensive SHM system was installed concurrently with the construction process. The composition of the SHM system and sensor numbering are illustrated in Fig. 4. The strain acquisition system comprises a total of 58 vibrating wire strain gauges, primarily located on the vertical members of Tower A, with each strain sensor accompanied by a temperature

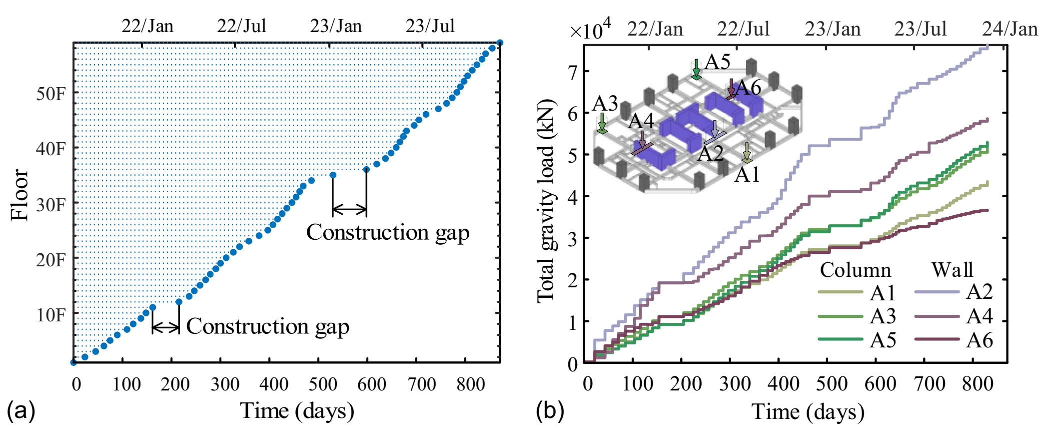

Fig. 3. Construction sequence and load of Tower A.

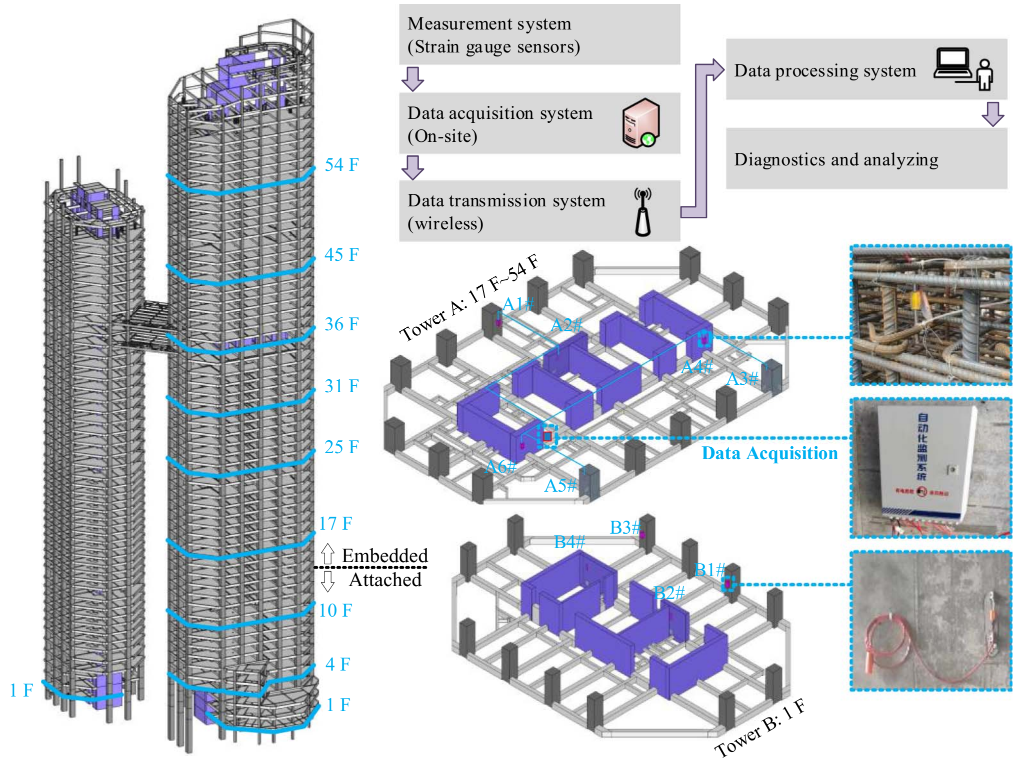

Fig. 4. Strain monitoring system.

sensor. At each floor where sensors were deployed, a data acquisition device was installed to facilitate remote data collection via wireless communication. Because the SHM system was implemented after Tower A was already under construction and had progressed to the 16th story, strain sensors were installed on the 1st, 4th, and 10th floors, while sensors above the 10th floor were pre-embedded within the vertical members to capture their complete deformation process. Six strain sensors were installed on each floor, monitoring three sets of vertical members.

Due to the complex and uncertain environment conditions at the construction site, the data acquisition devices could not be installed during the initial casting of the members. Installation of the devices required the removal of the concrete formwork and meeting specific site conditions. Therefore, before casting, data cables from the sensors were led out from the top slab of the story. On the day of casting, initial data from the strain sensors were manually collected on-site to avoid disturbances caused by concrete casting, as shown in Fig. 5. Subsequently, early strain data were manually collected on-site intermittently. Once the site conditions were met, wireless data acquisition devices were installed to obtain continuous strain data. The wireless communication sampling frequency was fixed at 10 min per reading. Additionally, accelerometer sensors were installed at the four corner points of the floor. The section form and reinforcement of the vertical members on the test floors are detailed in Appendix I.

Data Results and Preprocessing Analysis

Strain and Temperature Data

Initial strain measurements of the vertical members required manual readings, resulting in a lower frequency of strain data during the early stages of casting. High-frequency strain data could only be obtained after the installation of wireless acquisition devices, contingent on site conditions. Thus, the collected format is as shown in Fig. 6, which provides strain and temperature data for a set of vertical members on the 17th floor, spanning from the start of casting until nearly 2 years after the structure's topping out. Figs. 6(a and b) respectively depict the collected data for the locations of a column (A17-1) and wall (A17-2). It is evident that strains increase rapidly during the initial casting period, with columns exhibiting larger axial deformations than walls. The strain development exhibits a plateau between Days 200 and 300, which corresponds to periods of construction downtime, indicating that the monitoring data align well with the actual construction process. Additionally, the temperature data show a complete sinusoidal waveform, reflecting seasonal variations.

Data Preprocessing

Differences in thermal expansion coefficients between sensors and concrete create challenges in practically applying the raw data obtained directly from the sensors. as well as the inconsistent data collection frequency between manually collected early-stage data and the subsequent automated data. Additionally, the automated data collection often suffers from noise interference stemming from construction or environmental change, making the analysis of strain data inconvenient. Therefore, data processing procedures are imperative to facilitate the subsequent use of the data.

Exclusion of Temperature Effects

Due to complex on-site conditions and the lack of temperature compensation, the measured strain data include variations caused by temperature-induced deformations. At time t, the strain induced by temperature in concrete is deducted, as represented in Eq. (1)

$$\varepsilon(t) = \varepsilon_m(t) - [T(t) - T(0)] \cdot \Delta\alpha_t \tag{1}$$

J. Struct. Eng., 2025, 151(5): 04025044

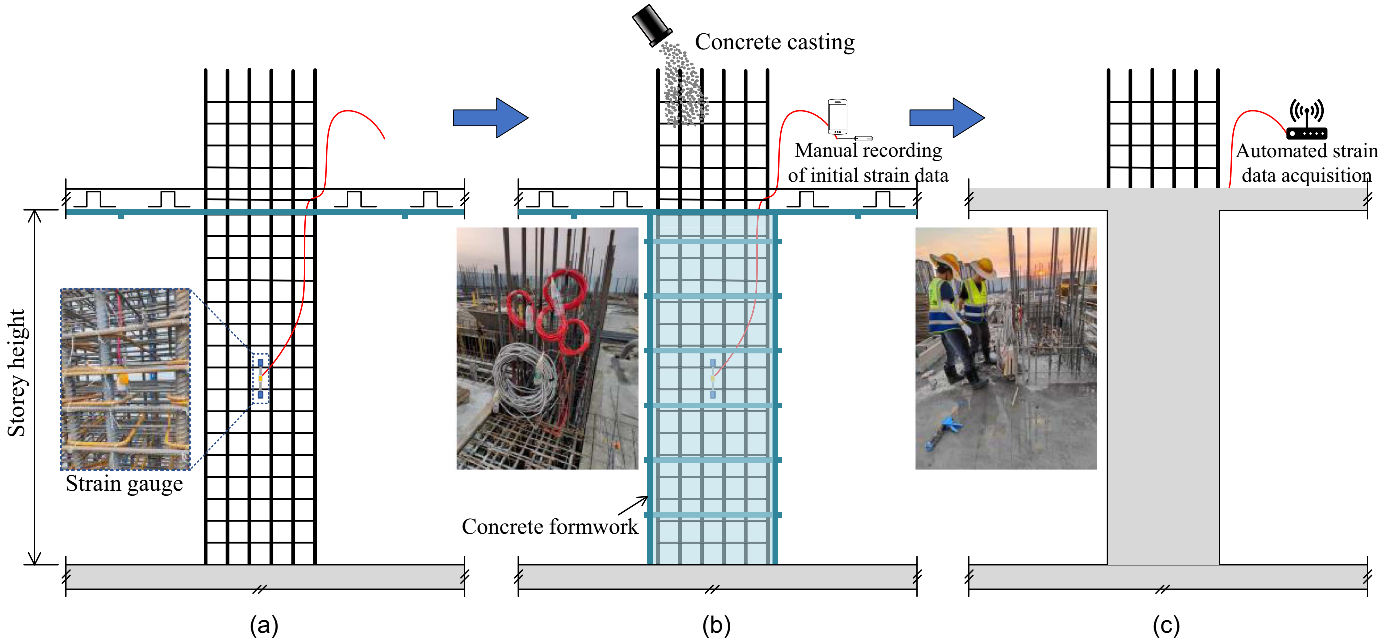

Fig. 5. Strain gauge pre-embedment and data acquisition schematic: (a) placement of sensors before concrete casting; (b) initial data collection during concrete casting; and (c) continuous automated strain data collection.

where ε = strain exclusive of temperature-induced effects, encompassing solely the shrinkage strain and the stress-dependent strain; ε_m = measured strain; T = sensor's temperature; and $\Delta\alpha_t = \alpha_{ts} - \alpha_{tc}$ represents the linear expansion coefficient difference between the sensor and concrete. Notably, $\Delta\alpha_t$ is set at 3 $\mu\varepsilon$/°C based on equipment recommendations and data conditions. Using data from Sensor A17-1 as an illustration, Fig. 7 presents the strain results before and after temperature correction. It is apparent from the localized strain data that after the temperature correction, the strain's sensitivity to temperature variations diminishes.

Data Smoothing and Reconstruction

The strain and temperature data collected remotely by the SHM system are susceptible to significant noise attributed to construction activities and environmental change. However, these noise effects on the axial deformation of vertical members can be practically disregarded. To facilitate research, data denoising and smoothing is essential. Additionally, due to the inconsistent data acquisition frequency before and after automatic collection, data resampling is required. In this study, the Savitzky–Golay (SG) filtering (Savitzky and Golay 1964) algorithm was employed to process the strain data. The core ideal of this algorithm involves weighted filtering of data within a window by fitting a high-order polynomial using least-squares regression to determine the weighted coefficients. Specifically, it filters $2n+1$ observations before and after time t by fitting a $k-1$ order polynomial, as follows:

$$x_t = a_0 + a_1 \cdot t + a_2 \cdot t^2 + \ldots + a_{k-1} \cdot t^{k-1} \tag{2}$$

This equation can also be used to predict values before and after the given time, forming $2n+1$ polynomials, combined to create the following matrix, where e represents the error between the fitted and measured values:

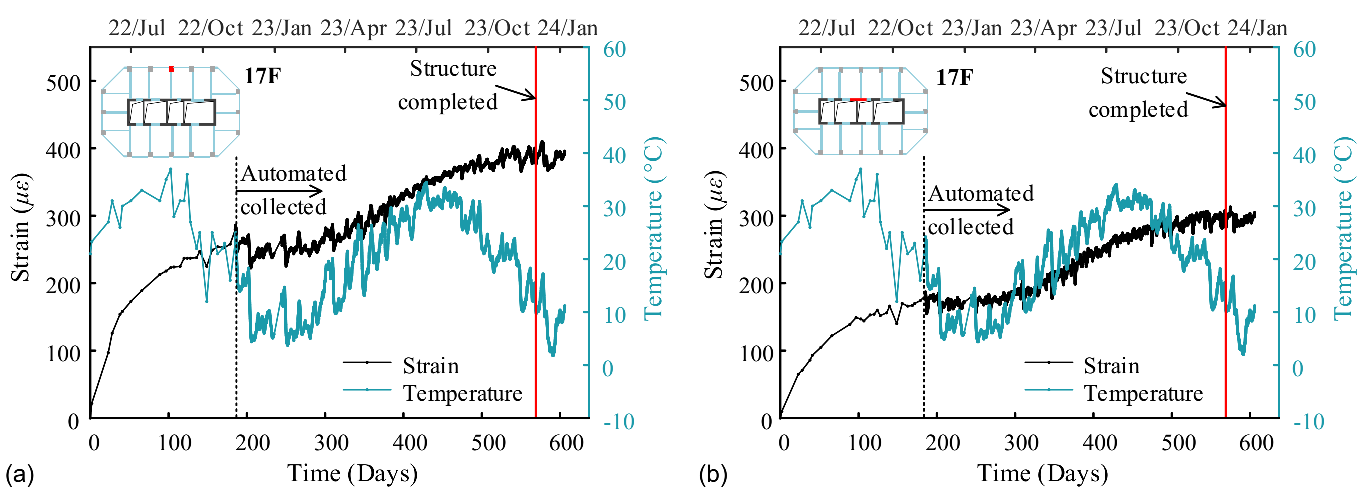

Fig. 6. Strain and temperature data: (a) A17-1; and (b) A17-2.

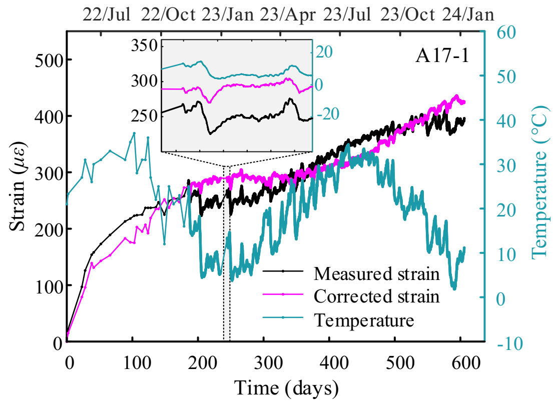

Fig. 7. Temperature-corrected strain.

$$\begin{bmatrix} x_{t-n} \\ \vdots \\ x_{t-1} \\ x_t \\ x_{t+1} \\ \vdots \\ x_{t+n} \end{bmatrix} = \begin{bmatrix} 1 & t-n & (t-n)^2 & \cdots & (t-n)^{k-1} \\ \vdots & \vdots & \vdots & \vdots & \vdots \\ 1 & t-1 & (t-1)^2 & \cdots & (t-1)^{k-1} \\ 1 & t & t^2 & \cdots & t^{k-1} \\ 1 & t+1 & (t+1)^2 & \cdots & (t+1)^{k-1} \\ \vdots & \vdots & \vdots & \vdots & \vdots \\ 1 & t+n & (t+n)^2 & \cdots & (t+n)^{k-1} \end{bmatrix} \begin{bmatrix} a_0 \\ a_1 \\ a_2 \\ \vdots \\ a_{k-1} \end{bmatrix} + \begin{bmatrix} e_{t-n} \\ \vdots \\ e_{t-1} \\ e_t \\ e_{t+1} \\ \vdots \\ e_{t+n} \end{bmatrix} \tag{3}$$

This equation can also be written as $\boldsymbol{X} = \boldsymbol{TA} + \boldsymbol{E}$. By applying the least-squares method, the coefficient matrix $\boldsymbol{A}$ can be calculated as

$$A = (\boldsymbol{T}^{\mathrm{T}} \cdot \boldsymbol{T})^{-1} \cdot \boldsymbol{T}^{\mathrm{T}} \cdot X \tag{4}$$

The model filtering value $\boldsymbol{P}$ is then obtained as

$$\boldsymbol{P} = \boldsymbol{T} \cdot \boldsymbol{A} = \boldsymbol{T} \cdot (\boldsymbol{T}^{\mathrm{T}} \cdot \boldsymbol{T})^{-1} \cdot \boldsymbol{T}^{\mathrm{T}} \cdot X \tag{5}$$

In this study, the polynomial degree was set to 3. For manually collected data, the filtering window size was chosen as 8, while for data automatically collected by the SHM system, the filtering window size was set to 10,000. After filtering the data, the frequency of the collected data remains inconsistent. Therefore, all data were resampled at a frequency of 10 days. The processed results are presented in Fig. 8, demonstrating consistency with the original data.

Processed Strain Results

All strain sensor data for Tower A were processed using the methods described previously, as shown in Fig. 9. The red line in the figure represents the topping out date, with 0 days indicating the start date of casting for the first floor. Due to uncertainties such as vibration during construction or formwork removal, some sensors were damaged. Overall, the strain data show rapid development in the early stages of casting. Notably, there is a distinct plateau stage between December 2022 and February 2023. The overall strain data obtained align well with the actual construction process, demonstrating the rationality and reliability of the data.

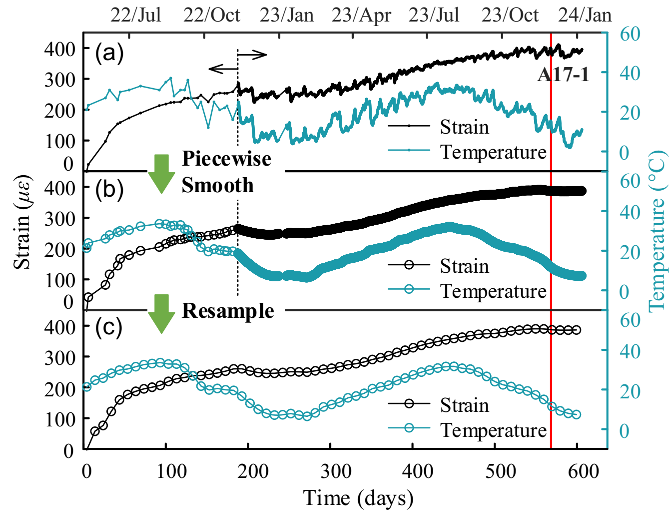

Fig. 8. Smoothed and resampled strain data.

Figs. 9(a and b) respectively show a set of adjacent vertical members at Positions 1 and 2, comparing the strain development at the 17th, 31st, and 36th stories. It is evident that the strain of the columns is significantly greater than that of the walls, which is consistent with previous related studies (Pfeifer et al. 1971; Wang et al. 2020; Fintel and Khan 1969; Wu et al. 2022). This is likely due to the lower volume-to-surface ratio and larger axial compression ratio of frame columns compared to shear walls, resulting in greater deformations from shrinkage and load-related effects. Figs. 9(c–f) present the measured strain results of two other sets of adjacent vertical members, it reveals a consistent strain development pattern, characterized by larger deformations in columns than in walls. Considering the vertical distribution of members within the structure, except for Position 1, the axial deformation development at the 36th story appears to be greater than at other floors. This is likely due to their location below the connecting story, which typically has a greater mass than the standard story.

Standard-Based Strain Calculation Results

Time-Dependent Characteristics of Concrete by Various Standards

The axial deformation of vertical members typically consists of two parts: stress-dependent and stress-independent deformation. Stress-dependent deformation includes elastic deformation and creep deformation, while stress-independent deformation refers to temperature and shrinkage. During the construction and service states, the vertical members of the structure are in the elastic stage ($\sigma < 0.4 f_c$). Therefore, the coordination between steel reinforcement and concrete deformation is maintained without relative slippage (Hubler et al. 2015; Mazloom 2008). Thus, only the time-dependent characteristics of concrete need to be considered. Scholars typically categorized the time-dependent characteristics of concrete under load into elastic deformation, shrinkage deformation, and creep deformation. Shrinkage deformation begins to develop from the casting of

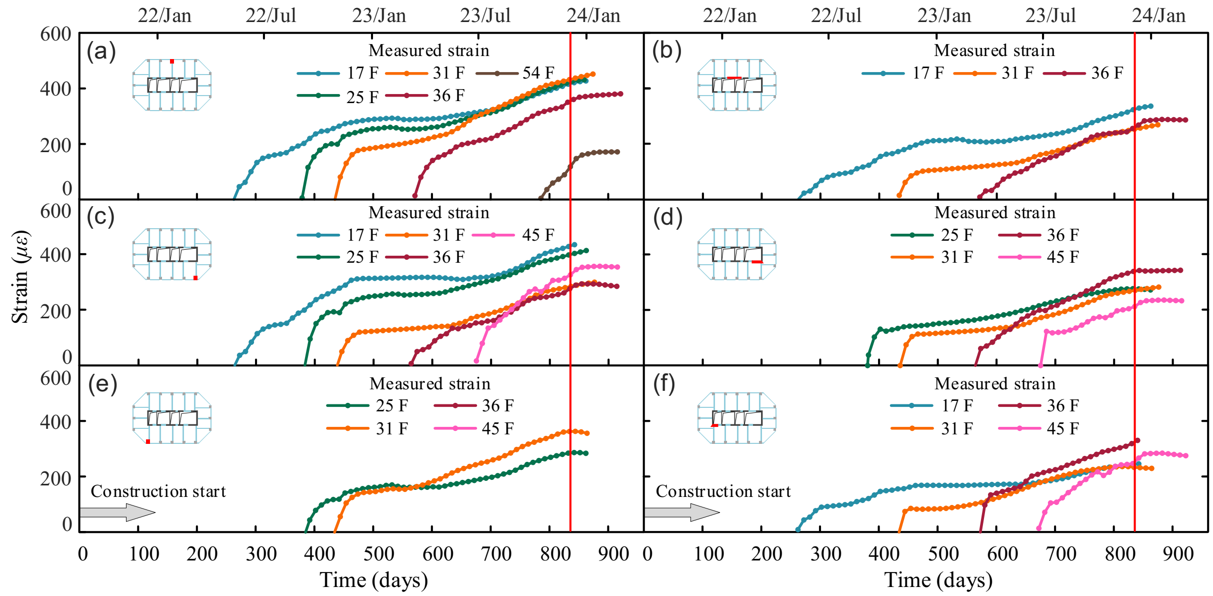

Fig. 9. Strain results overview: (a) Position A1; (b) Position A2; (c) Position A3; (d) Position A4; (e) Position A5; and (f) Position A6.

the concrete, while elastic deformation and creep deformation start from the moment the member is subjected to load. Unlike elastic deformation, creep deformation continues to increase for a considerable period after loading, but the rate of increase gradually slows down. Existing models separate these three types of deformation for calculation and then directly superpose according to the Boltzmann principle to obtain the total deformation of the component, as shown in Fig. 10.

MC2010 (CEB-FIP 2010) and ACI209R (ACI 1992) summarize scholars' research and provide equations for different time-dependent deformations of concrete. The B3 (Bažant and Murphy 1996) and GL2000 (Gardner and Lockman 2001) models are two widely recognized theoretical models for concrete shrinkage and creep. Appendix II lists the calculation equations for concrete elastic modulus, shrinkage, and creep for these four models.

Deformation Calculation in the Construction Stage

Current codes' and models' equations are derived from fitting shrinkage and creep test results of plain concrete. However, in practical engineering, plain concrete without reinforcement is typically nonexistent. During the construction stage, vertical members are subjected to cumulative loads, unlike the constant load in standard creep tests. Additionally, due to the complexity of vertical member

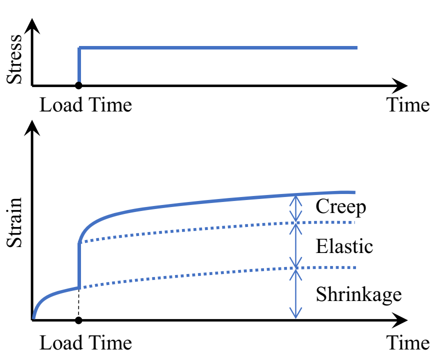

Fig. 10. Constituents of concrete deformation.

cross-sectional reinforcement and the vertical gravity loads during construction, the following assumptions and simplifications are necessary for deformation calculations of these members:

1. Ignoring bond slip between steel reinforcement and concrete, assume that the loads carried by both are distributed proportionally based on the cross-sectional area. Because vertical members typically have an axial compression ratio under 0.4 in service conditions, concrete remains in the elastic stage, where the deformation of steel reinforcement and concrete is essentially coordinated. Therefore, to consider the influence of steel reinforcement and for computational convenience, the elastic deformation can be expressed as

$$\varepsilon_e = \left(\frac{\rho}{E_s} + \frac{1-\rho}{E_c}\right)\sigma \tag{6}$$

where ε_e = elastic deformation; ρ = reinforcement ratio; E_s = modulus of elasticity of steel; E_c = modulus of elasticity of concrete; and σ = stress.

2. The influence of connected beam stiffness and outrigger trusses between vertical members on the axial deformation can be neglected. Horizontal connections between vertical members are typically through horizontal members or outrigger trusses in strengthened layers. However, the shear stiffness provided by horizontal members (such as beams and slabs) is significantly smaller than the stiffness required to prevent axial deformation of vertical members. Hence, the vertical members can be independently analyzed for axial forces (Elnimeiri and Joglekar 1989). Previous studies have indicated that outrigger trusses can reduce to some extent the impact of differential axial deformations (DASs) on the structure (Samarakkody et al. 2017; Kim et al. 2019; Kim 2017). However, in this project, the outrigger trusses were designed with a gap during initial construction to avoid additional internal forces due to DAS. The outrigger trusses were welded after the overall construction was completed, as shown in Fig. 11. Therefore, during the construction phase, the influence of the outrigger trusses can be disregarded, and the vertical members can be considered as independent elements subjected to axial forces.

J. Struct. Eng., 2025, 151(5): 04025044

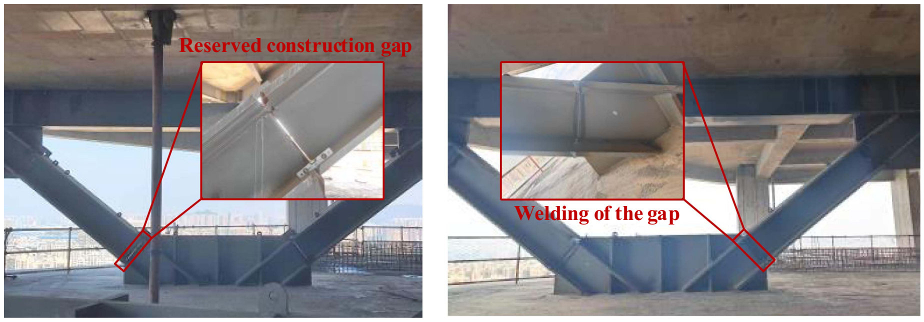

Fig. 11. Construction of outrigger truss.

3. Environmental loads-induced axial strains were disregarded, with sole consideration given to the incremental gravity loads from the upper levels. During structural construction, the axial strains in vertical members primarily result from the cumulative gravity loads imposed by the upper floors. The impact of environmental loads on these strains is negligible. Consequently, after excluding temperature-induced deformations, the strain data were treated as containing only elastic and creep deformations caused by concrete shrinkage and upper loads.
4. Each story load was considered as instantaneously applied, and the deformations generated by each story were directly superimposed for calculation. Although the increase in upper-story loads does not occur suddenly, concrete casting process is typically completed within a short period. Therefore, for computational convenience, the load on each story was modeled as a step function for analysis purposes.

Based on the assumptions and simplifications outlined, as well as the four models discussed in the previous section, vertical deformations of the members in this case were calculated. Taking Position 1 as an example, the computed results for each story are compared with the measured results in Fig. 12. The dashed lines in the figure represent the calculated results for unmonitored story. It can be observed that the results are generally of the same order of magnitude as the measurements, albeit with slight deviations. Among them, the MC2010 code aligns best with the measured results, especially the strain results at the 36th story. The calculated results trend from all models generally aligns with the measured trend for the 17th story within the first 500 days after casting, but after 500 days, the measured results are lower than the calculated results. This is likely due to the removal of temporary loads during the construction process, leading to lower measured strain compared with the constant loads considered in the calculations. The ACI 209R results show minimal deviation from MC2010 in terms of strain values, but both models' strain results for the 54th floor are higher than the measured results. The computed results from B3 and GL2000 are slightly higher than those from MC2010 and ACI 209R, showing larger deviations from the measured results. It is evident that existing models predict deformations with some deviation from the actual strain results. This discrepancy is attributed to the significant differences in the cross-sectional area and reinforcement ratio of vertical members compared to standard test specimens used to fit model parameters. Additionally, the complex construction conditions and the inability to maintain a constant environment on-site lead to significant deviations between concrete shrinkage and model's predicted results. Furthermore, construction materials at the construction site are typically randomly stacked, resulting in discrepancy between the loads used in calculations and the actual loads.

The calculation equations in models and codes often involve numerous parameters, such as concrete water-cement ratio and

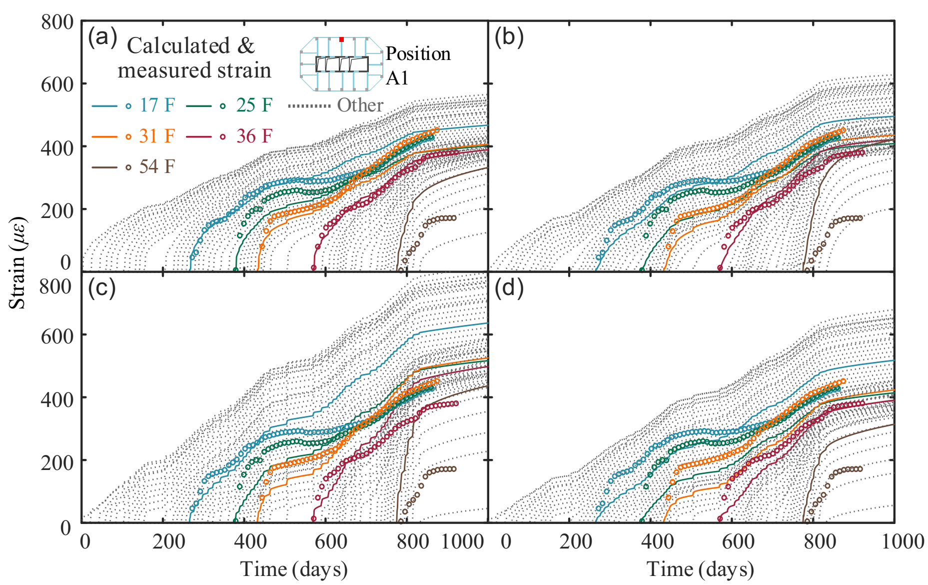

Fig. 12. Calculated and measured strain: (a) MC 2010; (b) ACI 209-R; (c) B3; and (d) GL2000.

J. Struct. Eng., 2025, 151(5): 04025044

slump, which are not obtainable during the design stage. Therefore, there is an urgent need to develop a more concise and physically meaningful time-dependent model for reinforced concrete.

Time-Dependent Models and Parameters Calibration

Fractional Order Viscoelasticity Model

FC (Hilfer 2000) refers to the operations of integration or differentiation involving noninteger orders. Fractional order viscoelastic models exhibit outstanding capabilities in describing the time-dependent deformation behavior of materials. Compared to traditional integer-order viscoelastic models, fractional order models excel in capturing long-term behavioral changes in materials and structures.

In the natural world, materials exhibiting pure elasticity or pure viscosity do not exist; the actual behavior always lies between these two properties. In rheology, pure elastic materials are symbolized as springs, adhering strictly to Hooke's law with a linear relationship between stress and strain. Purely viscous materials are represented as dashpots, adhering to Newton's law where stress and strain exhibit a linear relationship with the derivative with respect to time, as illustrated in Fig. 13. Researchers combine various basic elements to construct classical viscoelastic models such as Maxwell, Kelvin–Voigt, and the standard linear solid (SLS) to depict stress–strain relationships in a variety of materials. Due to each basic element containing a parameter, chain models derived from combining these elements possess numerous parameters, presenting challenges in deriving theoretical solutions or fitting experimental data accurately. Moreover, models composed of multiple basic elements often lack physical interpretation, hindering the intuitive representation of the deformation composition of each model component.

For viscoelastic materials, the constitutive equation of an ideal viscous material states that stress is proportional to the first-order derivative of strain with respect to time ($\sigma(t) \propto D^1\varepsilon(t)$, where D^χ denotes the χ th-order derivative with respect to time). In contrast, the constitutive equation of an ideal solid (spring) implies that stress is proportional to the zeroth-order derivative of strain with respect to time ($\sigma(t) \propto D^0\varepsilon(t)$). However, all real-world materials lie between solids and liquids (spring-pot); hence, stress in all materials is proportional to the zeroth- to first-order derivative

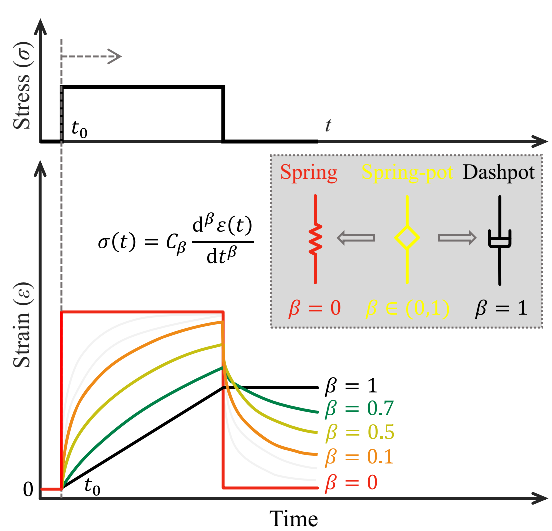

Fig. 13. Fractional order constitutive properties.

of strain with respect to time ($\sigma(t) \propto D^\beta\varepsilon(t)$, $\beta \in (0,1)$). Furthermore, the constitutive relationships of all material types can be expressed as

$$\sigma(t) = C_\beta \frac{d^\beta \varepsilon(t)}{dt^\beta} \tag{7}$$

where C_β = parameter of the material, where for an ideal elastic material $C_\beta = E$ (the elastic modulus), and for an ideal viscous material $C_\beta = \eta$ (the viscosity coefficient). The parameter β denotes the order of the material, where a value close to 1 signifies behavior more akin to an ideal viscous material, while values closer to 0 align with ideal elastic material characteristics.

For Eq. (7), when $\sigma(t) = \delta$ and considering the relevant definitions of FC, the analytical expression for the creep compliance of this model can be obtained (Schiessel et al. 1995)

$$J(t) = \frac{1}{C_\beta \Gamma(\beta + 1)} t^\beta \tag{8}$$

where Γ represents the gamma function, expressed as

$$\Gamma(\alpha) = \int_0^\infty e^{-t} t^{\alpha-1} \mathrm{d}t \tag{9}$$

Fig. 13 also illustrates the difference in strain response between the FC viscoelastic model with varying values of β and ideal solid and viscous materials under step load. It is evident that as the order β approaches 0, the strain response becomes closer to that of an ideal elastic body, while for higher values of β, it tends toward a more viscous behavior.

For the vertical members in this study, employing a single spring-pot element to simulate concrete time-dependent characteristics is evidently unsuitable. This model considers the component's deformation under loading, whereas in practical engineering members, deformation commonly comprises elastic, creep, and stress-independent deformation. Based on these characteristics, this study proposes the time-varying model for vertical components as shown in Fig. 14. This model comprises two springs, one spring-pot, and one shrinkage basic element. The spring-pot element represents concrete's creep deformation, which is connected in series with one spring unit (representing concrete's elastic deformation) and then in parallel with another spring unit (representing the elastic deformation of steel reinforcement). Finally, a concrete shrinkage element is arranged in series, related only to concrete material properties and time.

In the proposed model, k_c and k_s can be regarded as the stiffness provided by concrete and steel, respectively. For RC members, the elasticities can be simplified as

$$k_\beta = E_c(1 - \rho_s) \tag{10a}$$

$$k_\gamma = E_s \rho_s \tag{10b}$$

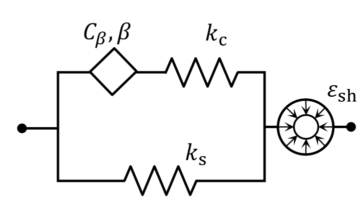

Fig. 14. Constitutive properties diagram.

J. Struct. Eng., 2025, 151(5): 04025044

where E_c and E_s = elastic modulus of concrete and steel, respectively; while ρ_s = cross-sectional reinforcement ratio.

Considering that this constitutive model is used to represent the axial deformation of vertical members and the deformation of the model is directly superimposed with the shrinkage element on the left side, the constitutive expression of the parallel model on the left side can be written as

$$\sigma_s(t) + \frac{C_\beta}{k_c}\frac{\mathrm{d}^\beta \sigma(t)}{\mathrm{d}t^\beta} = C_\beta \frac{\mathrm{d}^\beta \varepsilon_s(t)}{\mathrm{d}t^\beta} + \frac{C_\beta k_s}{k_c}\frac{\mathrm{d}^\beta \varepsilon_s(t)}{\mathrm{d}t^\beta} + k_s \varepsilon_s(t) \quad (11)$$

where $\varepsilon_s(t)$ = stress-dependent strain at time t. Letting $\sigma_s(t) = \delta(t)$ (Heaviside step function), the creep compliance function of the model can be obtained. Performing the Laplace transform and rearranging yields

$$\tilde{J}_s(s) = \tilde{\varepsilon}_s(s) = \frac{1}{s}\frac{k_c + C_\beta s^\beta}{C_\beta k_c s^\beta + C_\beta k_s s^\beta + k_c k_s} \quad (12)$$

Because both the creep and elastic deformations of concrete are linear, the overall strain of the model under constant axial force can be expressed as

$$\varepsilon(t) = J(t) \cdot \sigma + \varepsilon_{sh}(t) \quad (13)$$

The expression $J(t) = \mathcal{L}^{-1}[\tilde{J}_s(s)]$ cannot be explicitly written in the time domain. This study utilized the high-precision numerical integration method proposed by Talbot (1979) for the inverse Laplace transformation.

Bayesian Optimization of Parameters and Simulated Results

Based on the assumptions in the section "Deformation Calculation in the Construction Stage" and Eq. (13) for the time-varying deformation under constant axial force, the strain expression for the nth floor vertical member in this case during construction can be written as follows:

$$\varepsilon_n(t) = \sum_{t_i = t_{n+1}}^{t_{m-n}} J(t, t_i) \cdot \sigma(t_i) + \varepsilon_{sh}(t) \quad (14)$$

where m = total number of stories in the building; t_i = casting time for the ith story; $\sigma(t_i)$ = load induced by the upper casting at time t_i; and $J(t, t_i)$ = strain at time t resulting from the load at time t_i.

It is evident that this model comprises four parameters: C_β, β, k_c, and k_s. Among these, k_c and k_s can be obtained from Eq. (10). Hence, calibration is required for the parameters C_β and β. Given the relatively low dimensionality of the parameters, Bayesian optimization was employed in this study to determine the optimal values. Let the observed strain information be denoted as $\boldsymbol{Y}$ and the calculated strain as $\boldsymbol{Y}^*$. Based on the results from the existing model calculations, it is evident that MC2010 is relatively close to the measured results. Therefore, the shrinkage calculation equation from MC2010 is temporarily used for calculating ε_{sh}. The Bayesian parameter optimization process is illustrated in Fig. 15, and the loss function is constructed as the L2 norm of the difference between the calculated and measured values

$$\arg\min_{C_\beta,\beta} \boldsymbol{L}(C_\beta, \beta) = \arg\min_{C_\beta,\beta} \|\boldsymbol{Y} - \boldsymbol{Y}^*\|_2 \quad (15)$$

The results of $J(t, t_i)$ vary at different time instances t_i as the creep and elastic deformation of concrete decrease with the aging of concrete. Therefore, the calculation parameters for axial deformation induced by the load of each story in the upper part are different.

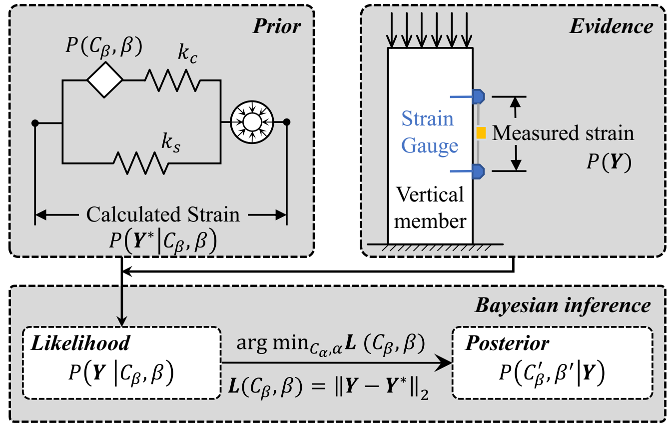

Fig. 15. Bayesian optimization workflow.

Based on the fitting analysis based on existing models, the results consistently show that the parameter β, representing the derivative order, is not significantly affected by concrete age. The primary influence is on the parameter C_β, and the regression analysis of the existing model's results yields the expression for C_β as

$$C_\beta(t_0) = k \cdot t_0^{0.14} \quad (16)$$

where k = parameter required in the Bayesian optimization process instead of C_β.

Upon optimizing the parameters of the vertical members based on the obtained strain data, the updated calculation results are presented in Fig. 16. It is evident that the calculated results of the proposed model closely approximate the measured strain data compared to existing models. However, some discrepancies between the calculated and measured strains still exist, notably in the strain results for the 17th floor at Position 1. This discrepancy is speculated to stem from variations in the vertical position of the crane between Vertical members 1 and 2 because the crane's vertical position changed after construction reached a certain level, resulting in differences between the actual and anticipated loads. Moreover, most of the calculated errors occur during the initial casting stages of the members. This is attributed to the susceptibility of vertical members to environmental disturbances and temporary loads during the initial curing stage. Notably, this issue is not exclusive to practical engineering but is also observed in laboratory experiments, where various models' predictions in the early curing and loading phases exhibit relatively lower accuracy compared to the mid-to-late stages (Zou et al. 2019; Ojdrovic and Zarghamee 1996). Nevertheless, the strain results for the remaining vertical members consistently align with the measured strains both in trend and values.

All optimized parameters are summarized in Appendix I. Vertical member parameters for different types and floors are depicted in Fig. 17. Notably, the parameter C_β predominantly ranges between 50,000 and 80,000, with wall parameters generally exceeding those of columns. Furthermore, C_β slightly exceeds the theoretical elastic modulus of concrete. Except for a few vertical members on the 17th floor, the parameter β fluctuates around 0.1. This indicates that the time-varying characteristics of concrete under external loads are closer to an ideal solid. Overall, the derived parameters fall within a reasonable range, demonstrating the method's applicability.

To analyze the composition parts and respective contributions to time-dependent deformations, the strains of each part in model are separated. For non-stress-related shrinkage deformations, which do not couple with other deformations, they can be directly separated.

J. Struct. Eng., 2025, 151(5): 04025044

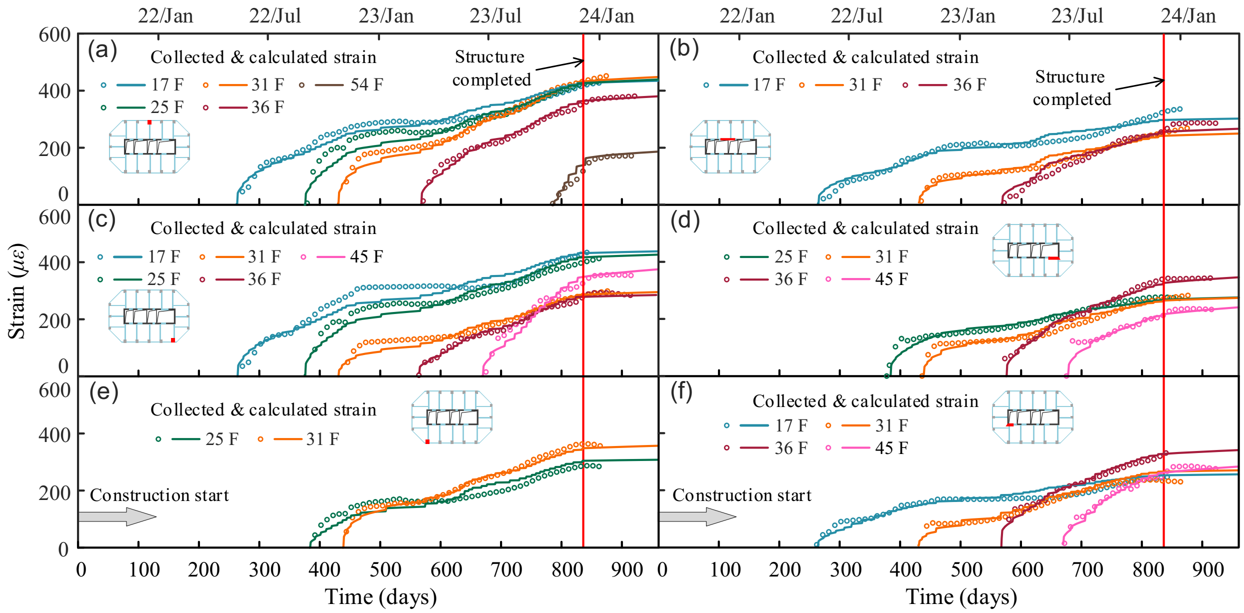

Fig. 16. Calculated versus measured results: (a) Position A1; (b) Position A2; (c) Position A3; (d) Position A4; (e) Position A5; and (f) Position A6.

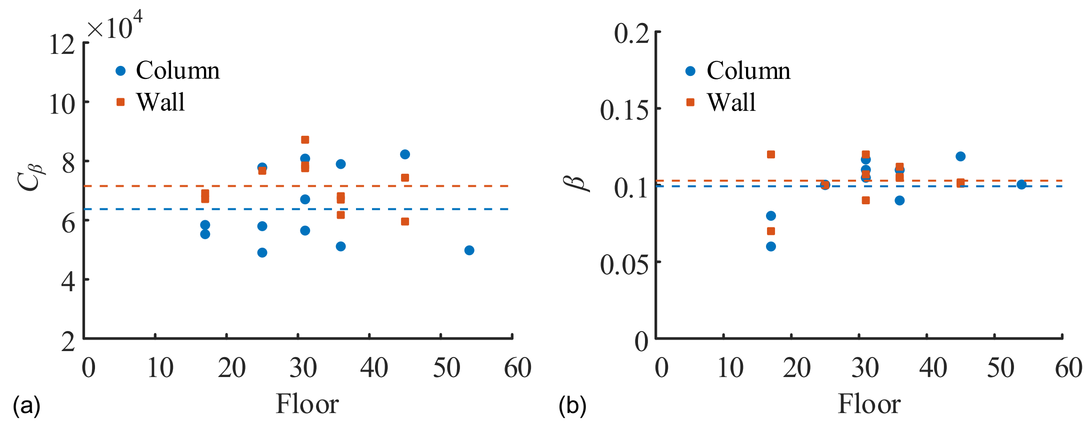

Fig. 17. Optimized parameters: (a) C_β; and (b) β.

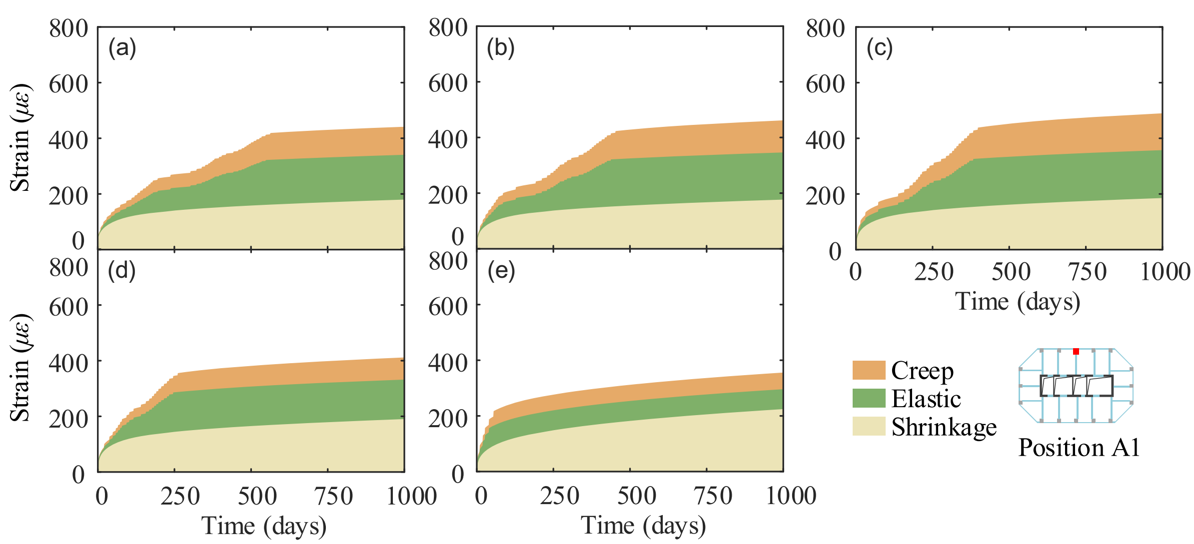

Fig. 18. Composition of deformation: (a) A17-1; (b) A25-1; (c) A31-1; (d) A36-1; and (e) A54-1.

However, in the model proposed in this study (Fig. 14), the elastic deformation of concrete, creep deformation, and elastic deformation of steel reinforcement are mutually coupled. In the process of calculating stress-dependent deformations $J(t)$, numerical methods are employed for the Laplace inverse transformation, as shown in Eq. (13). Therefore, it is not feasible to directly extract the individual components contributing to stress-related deformations during the solving process. Instead, the elastic deformations can be calculated using the equivalent elastic modulus, as shown in Eq. (6). Subtracting these elastic deformations from $J(t)$ yields the creep deformations. Although this approach may introduce slight discrepancies compared to actual computational results, it adequately fulfills analytical requirements.

Taking the example of Position 1 in Tower A, the composition of each part is illustrated in Fig. 18. It is evident that for higher floors, shrinkage deformation constitutes a larger proportion. This conclusion is straightforward because higher floors bear smaller upper loads, while shrinkage deformations are solely influenced by material properties. Additionally, the proportions of elastic deformation and creep deformation are generally similar, with creep deformation slightly less than elastic deformation. Therefore, it can be deduced that during construction, elastic deformation accounts for approximately half of the total deformation. This finding aligns with previous literature (Gao et al. 2020; Baker et al. 2007b). Hence, neglecting the time-dependent characteristics of concrete in structural deformation calculations is not reasonable.

Conclusions

This study explored the development of vertical member strains and their impact on structures during the construction of high-rise buildings. Utilizing strain monitoring data from a specific high-rise structure under construction, a viscoelastic model based on FC was proposed. This model notably enhances the rationality and precision of deformation simulations. The following is a summary of the research findings:

- During the construction of a high-rise twin tower asymmetric connected structure, a SHM system was installed to monitor the strain development of vertical members. A comparative analysis was conducted on the axial deformation differences of wall–column and the strain development process at different stories. It was observed that the trend of strain development remained consistent with the actual construction sequence, and the axial deformation of columns exceeded that of walls.
- By comparing the calculated results of different codes and existing models with measured data, it was found that MC2010 performed relatively well in predicting the strain development. However, there were still significant deviations from the measured results. The existing code requires numerous parameters, some of which are challenging to obtain during the design or construction stage, limiting its engineering applicability.
- A time-dependent constitutive model based on FC was proposed, characterized by clear physical interpretation, and requiring fewer parameters. Each element in the model distinctly represents the various components of deformation. For engineering or laboratory experiments, fitting can be performed separately, or a unified expression can be derived, simplifying and clarifying the calculation of axial deformation over time.
- By adjusting the model parameters using measured data and Bayesian optimization methods, the optimized model was employed to simulate axial deformation. Moreover, it enabled the prediction of vertical deformations caused by concrete shrinkage and creep decades after the service stage, significantly simplifying the assessment of concrete time-dependent effects on the structure.

Appendix I. Information and Optimized Parameters of Vertical Members

Strain sensor ID/type of specimen (column/wall)	Cross-sectional thickness of wall (mm)	Reinforcement ratio (%)	f_c (MPa)	Height (mm)	Optimized C_β	Optimized β
A1-1 (C)	1,800 × 2,000	6.09	60	4,800	—	—
A1-2 (W)	1,300	3.45			—	—
A1-3 (C)	1,800 × 2,000	5.96			—	—
A1-4 (W)	1,300	2.60			—	—
A1-5 (C)	1,800 × 2,000	5.96			—	—
A1-6 (W)	1,300	2.26			—	—
A4-1 (C)	1,800 × 2,000	6.09	60	4,500	—	—
A4-2 (W)	1,200	3.52			—	—
A4-3 (C)	1,800 × 2,000	5.96			—	—
A4-4 (W)	1,200	2.49			—	—
A4-5 (C)	1,800 × 2,000	5.96			—	—
A4-6 (W)	1,200	2.29			—	—
A10-1 (C)	1,700 × 1,900	5.40	60	4,100	—	—
A10-2 (W)	1,100	1.56			—	—
A10-3 (C)	1,700 × 1,900	5.40			—	—
A10-4 (W)	1,100	2.61			—	—
A10-5 (C)	1,700 × 1,900	5.40			—	—
A10-6 (W)	1,100	1.22			—	—
A17-1 (C)	1,700 × 1,900	0.95	60	4,100	55,271.46	0.08
A17-2 (W)	1,000	0.91			69,092.08	0.07
A17-3 (C)	1,700 × 1,900	5.40			58,401.15	0.06
A17-4 (W)	1,000	1.20			—	—
A17-5 (C)	1,700 × 1,900	5.40			—	—
A17-6 (W)	1,000	1.20			67,130.98	0.12

J. Struct. Eng., 2025, 151(5): 04025044

Appendix I. (*Continued.*)

Strain sensor ID/type of specimen (column/wall)	Cross-sectional thickness of wall (mm)	Reinforcement ratio (%)	f_c (MPa)	Height (mm)	Optimized C_β	Optimized β
A25-1 (C)	1,700 × 1,900	0.95	60	4,100	57,972.36	0.10
A25-2 (W)	1,000	1.41			—	—
A25-3 (C)	1,700 × 1,900	5.40			49,041.10	0.10
A25-4 (W)	1,000	4.42			76,701.34	0.10
A25-5 (C)	1,700 × 1,900	5.40			77,811.26	0.10
A25-6 (W)	1,000	3.53			—	—
A31-1 (C)	1,500 × 1,700	1.02	60	4,100	56,488.11	0.11
A31-2 (W)	800	0.94			78,487.43	0.12
A31-3 (C)	1,700 × 1,900	1.18			80,815.50	0.12
A31-4 (W)	800	1.23			77,569.16	0.11
A31-5 (C)	1,700 × 1,900	1.18			67,021.45	0.10
A31-6 (W)	800	1.21			87,186.23	0.09
A36-1 (C)	1,500 × 1,500	5.07	60	4,800	51,128.01	0.11
A36-2 (W)	700	1.44			68,108.50	0.11
A36-3 (C)	1,500 × 1,500	5.07			78,964.37	0.09
A36-4 (W)	700	3.39			61,759.28	0.10
A36-5 (C)	1,500 × 1,500	5.07			—	—
A36-6 (W)	700	4.16			66,953.05	0.11
A45-1 (C)	1,200 × 1,400	1.25	50	4,000	—	—
A45-2 (W)	500	1.27			—	—
A45-3 (C)	1,200 × 1,400	1.25			82,235.62	0.12
A45-4 (W)	500	1.27			74,341.96	0.10
A45-5 (C)	1,200 × 1,400	1.25			—	—
A45-6 (W)	500	1.27			59,548.93	0.10
A54-1 (C)	800 × 1,200	1.29	45	4,000	49,808.46	0.10
A54-2 (W)	400	1.26			—	—
A54-3 (C)	800 × 1,200	1.07			—	—
A54-4 (C)	800 × 1,200	1.07			—	—
A54-5 (C)	800 × 1,200	1.07			—	—
A54-6 (C)	800 × 1,200	1.38			—	—

Appendix II. Calculation Formulas for Various Standards and Models

Model	Contents	Calculation formulas
MC2010	Elastic modulus (MPa)	$E_c(t) = 21.5 \cdot 10^3 \cdot \left(\frac{f_{ct}(t)}{10}\right)^{1/3}; f_{ct}(t) = f_c \cdot \exp\left\{s_c \cdot \left[1 - \left(\frac{28}{t}\right)^{0.5}\right]\right\}$
	Shrinkage	$\varepsilon_{sh}(t, t_c) = -\alpha_{bs}\left(\frac{0.1 \cdot f_c}{6 + 0.1 \cdot f_c}\right)^{2.5} \cdot 10^{-6} \cdot (1 - \exp(-0.2 \cdot \sqrt{t})) + \varepsilon_{cds0} \cdot \beta_{RH} \cdot \beta_{ds}$
		$\varepsilon_{cds0} = [(220 + 110 \cdot \alpha_{ds1}) \cdot \exp(-\alpha_{ds2}) \cdot f_c] \cdot 10^{-6}$
	Creep	$\varphi(t, t_0) = \frac{1.8}{(f_c)^{0.7}} \cdot \ln\left(\left(\frac{30}{t_0} + 0.035\right)^2 \cdot (t - t_0) + 1\right) + \beta_{dc}(f_c) \cdot \beta(RH) \cdot \beta_{dc}(t_0) \cdot \beta_{dc}(t, t_0)$
ACI 209R	Elastic modulus (MPa)	$E_c(t) = 5{,}056\sqrt{f_{ct}(t)}; f_{ct}(t) = f_c \cdot \left(\frac{t}{a + bt}\right)$
	Shrinkage	$\varepsilon_{sh}(t, t_c) = \varepsilon_{shu} \cdot \left(\frac{t - t_c}{35 + (t - t_c)}\right)$
		$\varepsilon_{shu} = 780\gamma_{sh} \cdot 10^{-6}$
		$\gamma_{sh} = \gamma_{sh,tc} \cdot \gamma_{sh,RH} \cdot \gamma_{sh,vs} \cdot \gamma_{sh,s} \cdot \gamma_{sh,\psi} \cdot \gamma_{sh,c} \cdot \gamma_{sh,\alpha}$
	Creep	$\varphi(t, t_0) = \frac{(t - t_0)^{0.6}}{10 + (t - t_0)^{0.6}}\varphi_u$
		$\varphi_u = 2.35 \cdot \gamma_c$
		$\gamma_c = \gamma_{c,t0} \cdot \gamma_{c,RH} \cdot \gamma_{c,vs} \cdot \gamma_{c,s} \cdot \gamma_{c,\psi} \cdot \gamma_{c,\alpha}$

Appendix II. (*Continued.*)

Model	Contents	Calculation formulas
B3	Elastic modulus (MPa)	$E_c(t) = 4{,}734\sqrt{f_c}\left(\frac{t}{4+0.85t}\right)^{1/2}$
	Shrinkage	$\varepsilon_{sh}(t,t_c) = -\varepsilon_{shu}\cdot k_h\cdot S_s(t-t_c); \varepsilon_{shu} = -\varepsilon_{su}\frac{E_{ct}(607)}{E_{ct}(t_c+\tau_{sh})}$
		$\varepsilon_{su} = -\alpha_1\alpha_2[0.019w^{2.1}f_c^{-0.28}+270]\cdot 10^{-6}; S_s(t-t_c) = \tanh\left(\frac{t-t_c}{\tau_{sh}}\right)^{1/2}$
	Creep	$J(t,t_0) = \frac{127}{\sqrt{f_c}} + C_0(t,t_0) + C_d(t,t_0,t_c)$
		$C_0(t,t_0) = 185.4c^{0.5}f_c^{-0.9}Q(t,t_0) + 53.766\left(\frac{w}{c}\right)^4 c^{0.5}f_c^{-0.9}\cdot\ln[1+(t-t_0)^{0.1}] + 20.3(a/c)^{-0.7}\ln\left(\frac{t}{t_0}\right)$
		$C_d(t,t_0,t_c) = 7.57\cdot 10^5 f_c^{-1}\lvert\varepsilon_{shu}\rvert^{-0.6}\sqrt{\exp(-8H(t)) - \exp(-8H(t_0'))}$
		$\varphi(t,t_0) = E_c(t_0)J(t,t_0) - 1$
GL2000	Elastic modulus (MPa)	$E_c(t) = 3{,}500 + 4{,}300\sqrt{f_{ct}(t)}; f_{ct}(t) = f_c\cdot\left(\frac{t^{3/4}}{1+0.92t^{3/4}}\right)$
	Shrinkage	$\varepsilon_{sh}(t,t_c) = \varepsilon_{shu}\cdot\beta(h)\cdot\beta(t-t_c); \varepsilon_{shu} = 1{,}150\left(\frac{30}{f_c}\right)^{1/2}\times 10^{-6}$
		$\beta(t-t_c) = \left[\frac{(t-t_c)}{(t-t_c)+0.15(V/S)^2}\right]^{1/2}$
	Creep	$\varphi(t,t_0) = \Phi(t_c)\left[2\left(\frac{(t-t_0)^{0.3}}{(t-t_0)^{0.3}+14}\right) + \left(\frac{7}{t_0}\right)^{0.5}\left(\frac{t-t_0}{t-t_0+7}\right)^{0.5} + 2.5(1-1.086(RH/100)^2)\left(\frac{t-t_0}{t-t_0+0.15(V/S)^2}\right)^{0.5}\right]$
		$\Phi(t_c) = \left[1-\left(\frac{t_0-t_c}{t_0-t_c+0.15(V/S)^2}\right)^{0.5}\right]^{0.5}$

Note: The parameters in the equations were chosen according to conventional values: f_c = compressive strength of concrete under normal curing conditions after 28 days; t_c = starting time when the component is exposed to air; t_0 = time when load is applied; s_c, α_{bs}, α_{ds1}, α_{ds2} = coefficient for cement type; $h = 2A_c/u$; A_c = cross-sectional area; u = perimeter of the component in contact with the external environment; a, b = curing condition and the coefficient for cement type, respectively; k_h = humidity correction coefficient; and α_1, α_2 = constants related to the cement type and curing condition.

Data Availability Statement

All data, models, or codes that support the findings of this study are available from the corresponding author upon reasonable request.

Acknowledgments

The authors sincerely appreciate the funding support provided by the National Natural Science Foundation of China (NSFC) (Nos. 51878264 and 52278306), the Department of Science of Technology of Hunan Province (No. 2022SK2096), the Science and Technology Progress and Innovation Project of the Department of Transportation of Hunan Province (201912), the Natural Science Foundation of Hunan Province of China (Nos. 2023JJ70003 and 2024JJ6198), the Hydraulic Science of Technology Project of the Hunan Provincial Department of Water Resources (No. XSKJ2023059-31), and the Postgraduate Scientific Research Innovation Project of Hunan Province (No. CX20240459).

References

ACI (American Concrete Institute). 1992. *Prediction of creep, shrinkage, and temperature effects in concrete structures (209R-92)*. SP-076: 193–300. Farmington Hills, MI: ACI.

Baker, W. F., D. S. Korista, and L. C. Novak. 2007a. "Burj Dubai: Engineering the world's tallest building." *Struct. Des. Tall Spec.* 16 (4): 361–375. https://doi.org/10.1002/tal.418.

Baker, W. F., D. S. Korista, L. C. Novak, J. Pawlikowski, and B. Young. 2007b. "Creep and shrinkage and the design of supertall buildings—A case study: The Burj Dubai tower." *ACI J.* SP-246 (8): 133–148. https://doi.org/10.14359/18983.

Bal, L., and F. Buyle-Bodin. 2013. "Artificial neural network for predicting drying shrinkage of concrete." *Constr. Build. Mater.* 38 (Sep): 248–254. https://doi.org/10.1016/j.conbuildmat.2012.08.043.

Bažant, Z. P., and W. P. Murphy. 1996. "Creep and shrinkage prediction model for analysis and design of concrete structures-model B3." *Mater. Struct.* 28 (Jun): 357–365. https://doi.org/10.1007/BF02473152.

Bažant, Z. P., and L. Panula. 1978. "Practical prediction of time-dependent deformations of concrete." *Mater. Struct.* 12 (Sep): 169–183. https://doi.org/10.1007/BF02473872.

Bažant, Z. P., Q. Yu, and G. Li. 2012. "Excessive long-time deflections of prestressed box girders. I: Record-span bridge in Palau and other paradigms." *J. Struct. Eng.* 138 (6): 676–686. https://doi.org/10.1061/(ASCE)ST.1943-541X.0000487.

Beltempo, A., O. S. Bursi, C. Cappello, D. Zonta, and M. Zingales. 2018. "A viscoelastic model for the long-term deflection of segmental prestressed box girders." *Comput.-Aided Civ. Infrastruct. Eng.* 33 (1): 64–78. https://doi.org/10.1111/mice.12311.

Blanc, C. M., A. O. Sanchez, and I. F. Navarro. 2021. "Analytical characterisation of axial shortening due to creep of reinforced concrete columns in tall buildings." *Eng. Struct.* 228 (Feb): 111584. https://doi.org/10.1016/j.engstruct.2020.111584.

Bouras, Y., and Z. Vrcelj. 2023. "Fractional and fractal derivative-based creep models for concrete under constant and time-varying loading." *Constr. Build. Mater.* 367 (Jun): 130324. https://doi.org/10.1016/j.conbuildmat.2023.130324.

CEB-FIP (International Federation for Structural Concrete). 2010. *FIB model code for concrete structures 2010*. Berlin: *fib*. https://doi.org/10.1002/9783433604090.

Elnimeiri, M. M., and M. R. Joglekar. 1989. "Influence of column shortening in reinforced concrete and composite high-rise structures." *ACI J.* SP117 (4): 55–86. https://doi.org/10.14359/51687452.

Fan, F., H. Wang, X. Zhi, G. Huang, E. Zhu, and H. Wang. 2013. "Investigation of construction vertical deformation and pre-deformation control for three super high-rise buildings." *Adv. Struct. Eng.* 16 (11): 1885–1897. https://doi.org/10.1260/1369-4332.16.11.1885.

Fintel, M., S. K. Ghosh, and H. Iyengar. 1986. *Column shortening in tall buildings: Prediction and compensation*. Washington, DC: Portland Cement Association.

Fintel, M., and F. R. Khan. 1969. "Effects of column creep and shrinkage in tall structures prediction of inelastic column shortening." *ACI J.* 66 (12): 957–967. https://doi.org/10.14359/7444.

Gandomi, A. H., S. Sajedi, B. Kiani, and Q. Huang. 2016. "Genetic programming for experimental big data mining: A case study on concrete creep formulation." *Autom. Constr.* 70 (Jan): 89–97. https://doi.org/10.1016/j.autcon.2016.06.010.

Gao, F., H. Zhou, H. Liang, S. Weng, and H. Zhu. 2020. "Structural deformation monitoring and numerical simulation of a supertall building during construction stage." *Eng. Struct.* 209 (Sep): 110033. https://doi.org/10.1016/j.engstruct.2019.110033.

Gardner, N. J., and M. J. Lockman. 2001. "Design provisions for drying shrinkage and creep of normal-strength concrete." *ACI Mater. J.* 98 (2): 159–167. https://doi.org/10.14359/10199.

Glisic, B., D. Inaudi, J. M. Lau, and C. C. Fong. 2013. "Ten-year monitoring of high-rise building columns using long-gauge fiber optic sensors." *Smart Mater. Struct.* 22 (5): 055030. https://doi.org/10.1088/0964-1726/22/5/055030.

Havlásek, P., V. Šmilauer, L. Dohnalová, and R. Sovják. 2021. "Shrinkage-induced deformations and creep of structural concrete: 1-year measurements and numerical prediction." *Cem. Concr. Res.* 144 (Jun): 106402. https://doi.org/10.1016/j.cemconres.2021.106402.

Hilfer, R. 2000. *Applications of fractional calculus in physics*. Singapore: World Scientific. https://doi.org/10.1142/3779.

Hubler, M. H., R. Wendner, and Z. P. Bažant. 2015. "Comprehensive database for concrete creep and shrinkage: Analysis and recommendations for testing and recording." *ACI Mater. J.* 112 (4): 547. https://doi.org/10.14359/51687452.

Jayasinghe, M. T. R., and W. V. M. P. K. Jayasena. 2004. "Effects of axial shortening of columns on design and construction of tall reinforced concrete buildings." *Pract. Period. Struct. Des. Constr.* 9 (2): 70–78. https://doi.org/10.1061/(ASCE)1084-0680(2004)9:2(70).

Kang, F., J. Liu, J. Li, and S. Li. 2017. "Concrete dam deformation prediction model for health monitoring based on extreme learning machine." *Struct. Control Health Monit.* 24 (10): e1997. https://doi.org/10.1002/stc.1997.

Kim, H. S. 2017. "Optimum design of outriggers in a tall building by alternating nonlinear programming." *Eng. Struct.* 150 (Jun): 91–97. https://doi.org/10.1016/j.engstruct.2017.07.043.

Kim, H. S., H. Lee, and Y. Lim. 2019. "Multi-objective optimization of dual-purpose outriggers in tall buildings to reduce lateral displacement and differential axial shortening." *Eng. Struct.* 189 (Jul): 296–308. https://doi.org/10.1016/j.engstruct.2019.03.098.

Kurc, O., and A. Lulec. 2013. "A comparative study on different analysis approaches for estimating the axial loads on columns and structural walls at tall buildings." *Struct. Des. Tall Spec.* 22 (6): 485–499. https://doi.org/10.1002/tal.699.

Kwak, H. G., and J. K. Kim. 2006. "Time-dependent analysis of RC frame structures considering construction sequences." *Build. Environ.* 41 (10): 1423–1434. https://doi.org/10.1016/j.buildenv.2005.05.013.

Li, Q., Y. He, H. Wang, K. Zhou, and B. Yan. 2017. "Monitoring and time-dependent analysis of vertical deformations of the tallest building in China." *Struct. Control Health Monit.* 24 (7): e1936. https://doi.org/10.1002/stc.1936.

Maru, S., M. Asfaw, and A. K. Nagpal. 2001. "Consistent procedure for creep and shrinkage effects in RC frames." *J. Struct. Eng.* 127 (7): 726–732. https://doi.org/10.1061/(ASCE)0733-9445(2001)127:7(726).

Mazloom, M. 2008. "Estimating long-term creep and shrinkage of high-strength concrete." *Cem. Concr. Compos.* 30 (4): 316–326. https://doi.org/10.1016/j.cemconcomp.2007.09.006.

Moragaspitiya, P., D. Thambiratnam, N. Perera, and T. Chan. 2010. "A numerical method to quantify differential axial shortening in concrete buildings." *Eng. Struct.* 32 (8): 2310–2317. https://doi.org/10.1016/j.engstruct.2010.04.006.

Ojdrovic, R. P., and M. S. Zarghamee. 1996. "Concrete creep and shrinkage prediction from short-term." *ACI Mater. J.* 93 (2): 169–177. https://doi.org/10.14359/1416.

Pan, L. B., P. C. Liu, and S. L. Bakoss. 1992. "Long-term shortening of concrete columns in tall buildings." *J. Struct. Eng.* 119 (7): 2258–2262. https://doi.org/10.1061/(ASCE)0733-9445(1993)119:7(2258).

Pereira, M., and B. Glisic. 2023. "Calibration strategies for long-term strain forecasting in high-rise building columns." *Struct. Health Monit.* 23 (5): 2653–2678. https://doi.org/10.1177/14759217231207762.

Pfeifer, D. W., D. D. Magura, H. G. Russell, and W. G. Corley. 1971. "Time dependent deformations in a 70 story structure." *ACI J.* SP 27-7 (Sep): 159–186. https://doi.org/10.14359/17181.

Prakash, G., A. Sadhu, S. Narasimhan, and J. Brehe. 2018. "Initial service life data towards structural health monitoring of a concrete arch dam." *Struct. Control Health Monit.* 25 (1): e2036. https://doi.org/10.1002/stc.2036.

Praveen Moragaspitiya, H. N., D. P. Thambiratnam, N. J. Perera, and T. H. T. Chan. 2013. "Development of a vibration based method to update axial shortening of vertical load bearing elements in reinforced concrete buildings." *Eng. Struct.* 46 (Jun): 49–61. https://doi.org/10.1016/j.engstruct.2012.07.010.

Russell, H. G., and W. G. Corley. 1978. "Time-dependent behavior of columns in water tower place." *ACI J.* SP 55-14 (Jul): 347–374. https://doi.org/10.14359/6620.

Russell, H. W. 1980. *Field instrumentation of concrete structures*, 63–77. West Conshohocken, PA: ASTM. https://doi.org/10.1520/STP27139S.

Samarakkody, D. I., D. P. Thambiratnam, T. H. T. Chan, and P. H. N. Moragaspitiya. 2017. "Outrigger-belt and frame interaction in composite tall buildings under differential axial shortening." *J. Archit. Eng.* 23 (3): 04017016. https://doi.org/10.1061/(ASCE)AE.1943-5568.0000243.

Savitzky, A., and M. J. E. Golay. 1964. "Smoothing and differentiation of data by simplified least squares procedures." *Anal. Chem.* 36 (8): 1627–1639. https://doi.org/10.1021/ac60214a047.

Schiessel, H., R. Metzler, A. Blumen, and T. F. Nonnenmacher. 1995. "Generalized viscoelastic models: Their fractional equations with solutions." *J. Phys. A: Math. Gen.* 28 (23): 6567. https://doi.org/10.1088/0305-4470/28/23/012.

Sharma, R. K., S. Maru, and A. K. Nagpal. 2004. "Simplified procedure for creep and shrinkage effects in reinforced concrete frames." *J. Struct. Eng.* 130 (10): 1545–1552. https://doi.org/10.1061/(ASCE)0733-9445(2004)130:10(1545).

Shen, D., C. Li, C. Liu, M. Li, and J. Kang. 2020. "Experimental investigations on early-age tensile creep of internally cured high strength concrete under different initial stress/strength ratios." *Constr. Build. Mater.* 265 (Mar): 120313. https://doi.org/10.1016/j.conbuildmat.2020.120313.

Sortis, A. D., and P. Paoliani. 2007. "Statistical analysis and structural identification in concrete dam monitoring." *Eng. Struct.* 29 (1): 110–120. https://doi.org/10.1016/j.engstruct.2006.04.022.

Su, H., Z. Wen, X. Sun, and M. Yang. 2015. "Time-varying identification model for dam behavior considering structural reinforcement." *Struct. Saf.* 57 (Feb): 1–7. https://doi.org/10.1016/j.strusafe.2015.07.002.

Su, J., et al. 2013. "Long-term structural performance monitoring system for the Shanghai tower." *J. Civ. Struct. Health Monit.* 3 (1): 49–61. https://doi.org/10.1007/s13349-012-0034-z.

Talbot, A. 1979. “The accurate numerical inversion of Laplace transforms.” *IMA J. Appl. Math.* 23 (1): 97–120. https://doi.org/10.1093/imamat/23.1.97.

Wang, L., X. Zhao, and C. Yan. 2020. “Time-dependent vertical shortening prediction for super-tall buildings by using a modified B3 model to consider moisture distribution.” *Eng. Struct.* 209 (May): 109994. https://doi.org/10.1016/j.engstruct.2019.109994.

Wendner, R., M. H. Hubler, and Z. P. Bažant. 2013. “The B4 model for multi-decade creep and shrinkage prediction.” In *Proc., 9th Int. Conf. on Creep, Shrinkage, and Durability Mechanics (CONCREEP-9)*, 429–436. Reston, VA: ASCE. https://doi.org/10.1061/9780784413111.051.

Wu, J., C. Pang, and B. Dong. 2022. “Dual compensation method for vertical shortening -and differential shortening control in high-rise buildings.” *J. Build. Eng.* 57 (Nov): 104967. https://doi.org/10.1016/j.jobe.2022.104967.

Xia, Y., Y. Ni, P. Zhang, W. Liao, and J. Ko. 2011. “Stress development of a supertall structure during construction: Field monitoring and numerical analysis.” *Comput.-Aided Civ. Infrastruct. Eng.* 26 (7): 542–559. https://doi.org/10.1111/j.1467-8667.2010.00714.x.

Zhou, Y., X. Luo, P. Ye, W. Zhang, L. Qin, and Z. Du. 2023. “Bayesian-based prediction and real-time updating of axial deformation in high-rise buildings during construction.” *Eng. Struct.* 297 (Dec): 116992. https://doi.org/10.1016/j.engstruct.2023.116992.

Zhou, Y., X. Luo, W. Zhang, P. Ye, J. Chen, and Z. Du. 2024. “Improvement of axial deformation prediction in high-rise buildings with filed monitoring and adaptive unscented Kalman filter.” *J. Build. Eng.* 83 (May): 108432. https://doi.org/10.1016/j.jobe.2023.108432.

Zhu, H., K. Gao, Y. Xia, and Q. Hu. 2019. “Multi-rate data fusion for dynamic displacement measurement of beam-like supertall structures using acceleration and strain sensors.” *Struct. Health Monit.* 19 (2): 520–536. https://doi.org/10.1177/1475921719857043.

Zhu, J., and Y. Wang. 2021. “Convolutional neural networks for predicting creep and shrinkage of concrete.” *Constr. Build. Mater.* 306 (Feb): 124868. https://doi.org/10.1016/j.conbuildmat.2021.124868.

Zou, D., C. Du, T. Liu, J. Teng, and H. Cheng. 2019. “Time-dependent deformations of concrete columns under different construction load histories.” *Adv. Struct. Eng.* 22 (8): 1845–1854. https://doi.org/10.1177/1369433219828133.